Applied Thermal Engineering 272 (2025) 126410

Contents lists available at ScienceDirect

Applied Thermal Engineering

journal homepage: www.elsevier.com/locate/apthermeng

Research Paper

A simple multiple flow regime modeling approach of induced flow in external loop airlift reactors☆

Bor Zupan [a], Matjaž Perpar [a], Jurij Gregorc [a], Božidar Šarler [a,b,*]

[a] Laboratory for Fluid Dynamics and Thermodynamics, Faculty of Mechanical Engineering, University of Ljubljana 1000 Ljubljana, Slovenia
[b] Laboratory for Simulation of Materials and Processes, Institute of Metals and Technology, Lepi pot 11, 1000 Ljubljana, Slovenia

ARTICLE INFO

Keywords:
Airlift reactor
Homogeneous flow
Separated flow
Theoretical model
Induced flow
Pressure loss

ABSTRACT

Accurate treatment of heat and mass transfer processes inside airlift reactors requires accurate velocity field information. This study presents a novel one-dimensional model forecasting induced liquid flow within an external loop airlift reactor across diverse flow regimes. The approach is grounded on homogeneous flow assumption, augmented by a novel correction term derived through modeling of turbulence-induced pressure losses behind gas structures, employing the separated flow model (Lockhart-Martinelli). The model was assessed by comparing the results with purpose-provided experimental data utilizing air and demineralized water. The gas and liquid superficial velocities ranged from 0.001-0.6 m/s and 0.2–1.1 m/s, respectively. Within ± 10 %, an agreement between the novel model and experimental data was observed for both bubbly, separated, and intermediate flow regimes. A similarly robust agreement was confirmed through comparisons with five published experimental datasets. The distinctive feature of this model is its ability to accommodate multiple flow regimes in a unified manner. It circumvents the necessity for specific regime modeling by introducing a correction term with a complexity marginally surpassing that of the conventional homogeneous flow approach. Beyond its primary application in airlift reactors, the model provides a unified framework for modeling two-phase flow hydrodynamics in thermal applications, particularly in flow boiling and bubble-induced convective heat transfer systems. The model's simple yet effective structure also allows for integration into higher-fidelity heat transfer simulations, making it valuable for boiling heat transfer studies, enhanced cooling strategies, and industrial multiphase flow applications.

1. Introduction

An airlift reactor (ALR) is a bioreactor similar to gaslift pumps [1], that utilizes the low density of a gaseous phase as the mixing force instead of a mechanical blade. It is characterized by its simple construction, absence of moving parts, and prominent mixing and mass transfer with low energy consumption [2]. The gaseous phase may either react during the process or remain inert. Based on their geometry, ALRs can be divided into two main types (Fig. 1): (a) internal loop airlift reactors (ILALRs) and (b) external loop airlift reactors (ELALRs). All ALRs consist of four separate sections with different flow characteristics, namely the *separator* (connects the riser and the downcomer at the top and ensures the gas phase is evacuated from the liquid phase), *riser* (where gas is injected via a sparger at the bottom), *downcomer* (usually parallel to the riser and consists mainly of a downward liquid flow), *base* (connects two conduits at the bottom of the reactor).

They are widely used in chemical and biochemical processes [3–10] due to their efficient mixing and low energy consumption. Their utilization of the buoyancy-driven liquid recirculation eliminates the need for mechanical agitation. The absence of moving parts reduces shear stress, making ALRs particularly suitable for shear-sensitive biological cultures [11–14]. ALRs are also commonly used in heat and mass-transfer-intensive processes, such as fermentation [15], wastewater treatment [16], and catalytic reactions [17], where maintaining thermal homogeneity is critical. However, despite their widespread application, the fundamental hydrodynamic and thermal interactions between flow regimes remain insufficiently explored. The ability to predict induced

Abbreviations: 1D, one-dimensional; ALR, Airlift Reactor; CFD, Computational Fluid Dynamics; ELALR, External Loop Airlift Reactor; HFM, Homogeneous flow model; ILALR, Internal Loop Airlift Reactor; PSDF, Power Spectral Density Function; SFM, Separated flow model; STR, Stirred-Tank Fermenters.

☆ This article is part of a special issue entitled: 'EUROTHERM2024' published in Applied Thermal Engineering.

* Corresponding author.
E-mail address: bozidar.sarler@fs.uni-lj.si (B. Šarler).

https://doi.org/10.1016/j.applthermaleng.2025.126410
Received 29 November 2024; Received in revised form 4 March 2025; Accepted 2 April 2025
Available online 5 April 2025

Nomenclature

Variable	Unit	Meaning
C_D	/	drag coefficient
C_∞	/	dimensionless drag constant
C_P	J kg^{-1} K^{-1}	specific heat capacity
D	m	duct diameter
D_H	m	hydraulic diameter
f	/	Fanning friction factor
g	m s^{-2}	gravitational acceleration
h	W m^{-2} K^{-1}	heat transfer coefficient
H	m	riser duct height
j	m s^{-1}	superficial velocity
k	W m^{-1} K^{-1}	thermal conductivity
K	/	minor pressure loss coefficient
$\dot{m}''$	kg m^{-2} s^{-1}	absolute mass flux
n	/	free parameter in HFM
Nu	/	Nusselt number
U*		expanded measurement uncertainty (*unit depends on the variable observed)
Pr	/	Prandtl number
ΔP	Pa	pressure difference
r_d	m	bubble radius
r_d^*	/	dimensionless bubble radius
Re	/	Reynolds number
w	ms^{-1}	phase velocity
x	/	mixture quality
X	/	Martinelli parameter
α	/	gas holdup
μ	Pa s	dynamic viscosity
ρ	kgm^3	density
σ	Nm^{-1}	surface tension
ε	/	reactor dissipation parameter
Φ	/	pressure drop multiplier

liquid velocity, gas holdup, and pressure losses is critical for designing ALRs that maximize heat and mass transfer efficiency. Understanding flow regimes allows for better control over convective heat transfer in reactors where heat generation or dissipation occurs. For instance, the interaction of gas bubbles with liquid flow fields strongly influences temperature distribution, turbulence, and local heat transfer coefficients, affecting system performance. Beyond ALRs, similar mechanisms are present in flow boiling systems [18], where bubble formation, growth, and detachment govern boiling heat transfer rates, as well as in bubble-enhanced heat exchangers [19], where dispersed gas phases are introduced to improve thermal performance.

Despite its advantages, ALRs present challenges in accurately predicting key process parameters, such as gas holdup, circulation velocity, and heat transfer rates, due to the complexity of two-phase flows and the interplay of geometric and operating variables. Reliable prediction of these parameters is essential for optimizing ALR design and performance, particularly for thermal processes where heat and mass transfer significantly influence efficiency. Many existing ALR models are either empirical or rely on flow regime-specific correlations, requiring separate formulations for different operating conditions. Computational Fluid Dynamics (CFD) simulations have improved understanding [20–33] but remain computationally expensive for industrial-scale applications. Furthermore, empirical and flow-pattern-specific models [34–38] often lack generalizability beyond their original experimental conditions. Camarasa et al. [35] showed that applying different gas holdup correlations per regime can improve accuracy, but this approach complicates the modeling process.

This study presents a unified theoretical model that predicts recirculating velocity across multiple flow regimes, eliminating the need for separate regime-specific treatments. The model incorporates an additional pressure loss term for turbulent wake dissipation, making it particularly relevant for systems where heat and mass transfer are closely coupled with multiphase flow behavior. Extending this modeling approach to thermally driven two-phase systems, such as flow boiling or

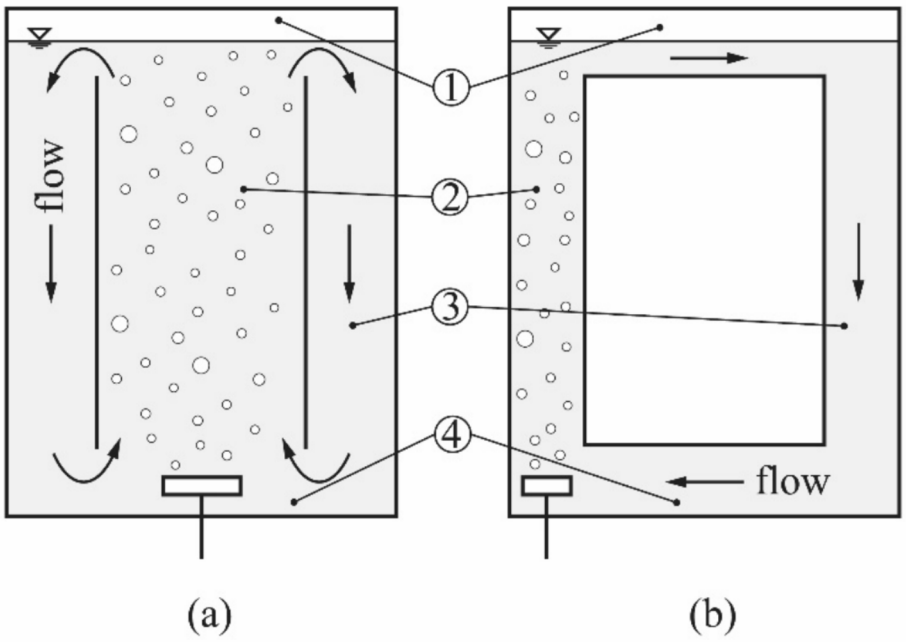

Fig. 1. Two main design types of airlift reactors: (a) internal loop airlift reactor and (b) external loop airlift reactor. Flow in the riser is directed upward. Labeled sections are: 1) separator, 2) riser, 3) downcomer, and 4) base. Gas is inserted through the sparger at the bottom of the riser.

heat transfer via bubble injection, provides a foundation for studying enhanced convective heat transfer. Possible further implications are.

- Enhanced Thermal Modeling: Accurate predictions of liquid recirculation velocity allow for precise evaluation of heat transfer rates, which are critical for processes requiring tight thermal control. These include biotechnological fermentations, chemical reactions, and catalytic operations where temperature plays a key role in reaction kinetics and product yield. The heat transfer rate can be, for instance, modeled by integrating the liquid velocity w_L into established heat transfer equations, such as the modified Dittus-Boelter equation [39] for convective heat transfer,

$$\mathrm{Nu} = \frac{h_L}{k_L} = C_1 \mathrm{Re}_L^{C_2} \mathrm{Pr}_L^{C_3} = C_1 \left(\frac{\rho_L w_L D_H}{\mu_L}\right)^{C_2} \left(\frac{C_{p,L}\mu_L}{k_L}\right)^{C_3}, \# \quad (1)$$

where Nu, Re, and Pr are the Nusselt, Reynolds, and Prandtl numbers, and h, k, ρ, D_H, μ and C_p are the heat transfer coefficient, thermal conductivity, density, hydraulic diameter, dynamic viscosity, and mass-specific heat capacity. Index L denotes the liquid phase. The parameters C_1, C_2 and C_3 are empirical constants and depend on the specific conditions of the system. For a turbulent flow in smooth pipes, typical values are $C_1 = 0.023$, $C_2 = 0.8$ and $C_3 = 0.3$ (heating) or $C_3 = 0.4$ (cooling) [40].

- Energy Efficiency and Process Optimization: The model provides a foundation for optimizing reactor energy efficiency by quantifying the reactor losses. Applications such as wastewater treatment, pharmaceutical manufacturing, and large-scale algal cultivation benefit from reduced operational costs and improved thermal performance.
- Integration into Coupled Models: The simplicity of this model makes it suitable for integration into more complex simulations that account for combined heat, mass, and momentum transfer. This versatility can help further explore how reactor designs and operating conditions impact thermal and mass transfer characteristics.

This study addresses the present research gap by developing a novel, comprehensive model of recirculating velocity in ELAIRs to reduce the complexity of the models already presented in the literature [34–38] while maintaining a good agreement with the various experimental data. As such, it offers simple implementation into more complex reactor heat and mass transfer models. In addition, another theoretical model capable of predicting the recirculating velocity in the separated-flow regime was developed to determine the value of a newly proposed parameter in the simpler model. The paper first outlines our experimental apparatus, where we could systematically measure the volumetric flow rates of the working fluids, pressure drops, and pressure fluctuations in the riser. A high-speed camera was used to capture the spatial and temporal development of the two-phase flow in the riser. The flow regimes were determined by a frequency analysis of the pressure fluctuation signals and confirmed by visual inspection. The primary objective of the experimental analysis was to capture different flow regimes for which a unified treatment could be established. The paper then provides a theoretical approach to liquid recirculating velocity modeling and develops it for the ELALR based on the principle of energy conservation. The model is assessed using our own published experimental data [38]. The newly developed model aims to accurately predict the induced recirculating flow of the carrier liquid phase over multiple flow regimes, namely the homogeneous and separated flow, in a simple manner. Consequent heat and mass transfer models can significantly benefit by using the proposed model as a starting point for hydrodynamical conditions inside the reactor.

2. Experiment

2.1. Experimental setup

Fig. 2 shows the experimental setup. It consists of a circular riser (I) and downcomer duct (II), both of which have an inside diameter of 40 mm. They are connected at the top and bottom using the separator (III) and base (IV). The riser is made of acrylic glass, which allows high-speed imaging along the duct. Imaging is performed using a movable rectangular box (8) filled with water to negate the effect of light refraction by the circular duct. The length of the riser is 2005 mm.

Compressed air (5) was used as the gaseous phase, and the gas flow rate was measured using a set of rotameters (4). Gas is introduced into the riser via six 1.6 mm holes located every 60° around the perimeter of the nozzle (6). The nozzle geometry is described in Fig. 2a. The liquid flow rate was measured using an ultrasonic flow meter (1) and was forwarded to a computer via an RS-485 to a USB-2 converter (7). The calculated superficial velocities of air and demineralized water ranged from 0 to 0.6 m/s and 0.2 to 1.1 m/s, respectively.

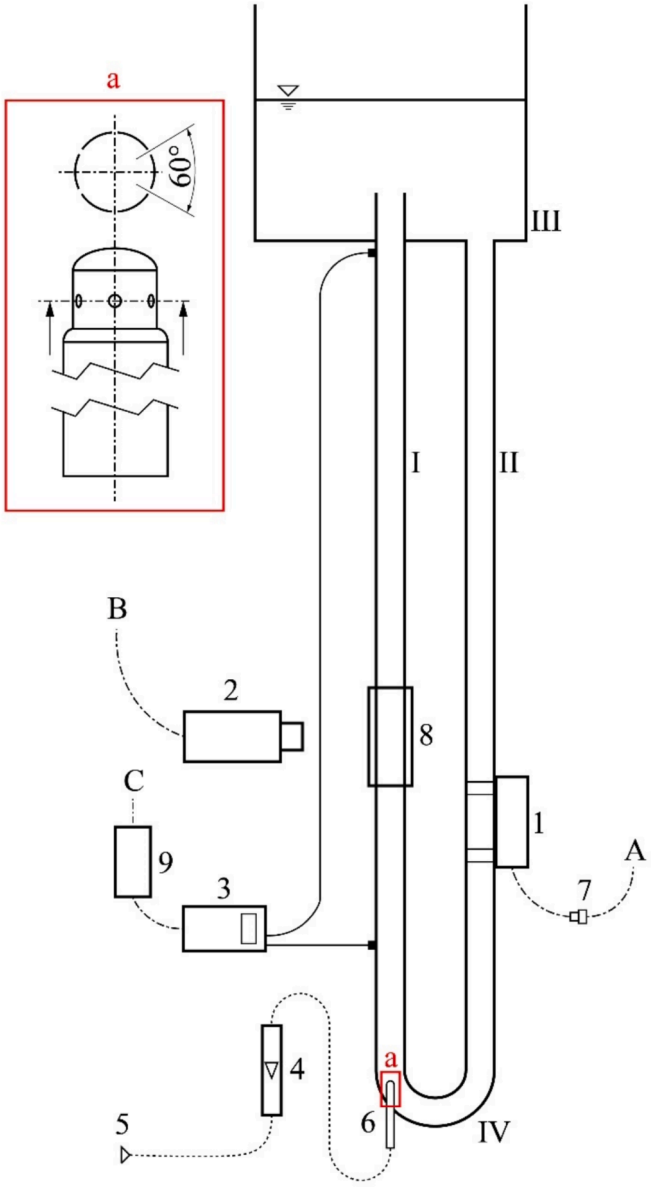

Fig. 2. Experimental setup scheme (not to scale). The geometry of the gas sparger is shown in detail a.

The flow regimes in the riser were imaged with a high-speed camera (2) capable of capturing 10 k frames per second (FPS) at three locations, specifically at 180, 1024, and 1719 mm from the top of the gas sparger. A set of two differential pressure sensors (3) were used to record the pressure drop and fluctuations in the riser. The height difference between the pressure sensors was 1917 mm. The analog signal was collected using a multifunctional I/O module (9). The letters A, B, and C represent the acquired signals for the liquid flow rate, video image, and pressure sensor values.

2.2. Measurement procedure and analysis

Video recordings were captured at 2 k FPS, with a 1024 × 768 pixel resolution and exposure time of 60 microseconds. Filming was conducted using the same camera at three locations along the riser to capture the spatial evolution of the flow. The pressure signal was sampled at a frequency of 1 kHz. Because of the transient nature of the flow, the signal was recorded for 60 s, resulting in the acquisition of 60 k data points. The signal was averaged over the entire dataset using Equation (2) to calculate the gas holdup. Spectral analysis of the pressure signal was performed using Fast Fourier Transform. The liquid flow rate in the downcomer was measured for 60 s at a frequency of 1 Hz using an ultrasonic flowmeter.

Gas holdup α was calculated as

$$\alpha = \frac{\Delta P_{R,\exp}}{(\rho_L - \rho_G)gH}, \# \tag{2}$$

where $\Delta P_{R,\exp}$ is the experimentally measured pressure difference between the two pressure probes in the riser, g is the gravitational constant, and $H = 1917$mm is the height difference between the probes. Indices L and G denote the liquid and gas phases, respectively. The experimental gas holdup was determined to be in the 0.02–0.19 range.

2.3. Average bubble size

To estimate the flow drag coefficient, high-speed footage of 19 cases with increasing gas holdup was analyzed and grouped into nine similar bubble-sized sets. The average bubble size was determined for each set via the average bubble chord length r_d. Measurements were transformed into dimensionless form via the non-dimensional radius $r_d^* = r_d \cdot \left(\rho_L g \Delta\rho \mu_L^{-2}\right)^{1/3}$, where $\Delta\rho = \rho_L - \rho_G$. When bubbles with $r_d^* > 10^2$ were measured, smaller bubbles in the Newton/viscous regime were omitted because their contribution was assumed to be negligible. In all cases, the drag coefficient of a large bubble ($r_d^* > 10^2$) was at least one order of magnitude larger than that of a small spherical bubble ($r_d^* < 3{\cdot}10^1$).

The bubble clusters were analyzed in the following way: where the clusters were complex, with turbulent bubble dynamics making direct bubble measurements impossible, the cluster was treated as a single distorted bubble entity. Such clusters were found at higher gas flow rates. However, even in these regimes, individual bubbles still comprised most of the riser domain. This cluster treatment was not applied to large cluster entities, which quickly transitioned into slug flow. At lower gas flow rates, clusters contained fewer distorted bubbles with well-resolved interfaces, allowing for individual bubble treatment. The characteristic bubble size was measured using the bubble chord length to account for bubble deformation. This approach is advantageous because it is compatible with visual footage analysis and in-situ techniques (e.g., conductivity probes) to which the drag force models were initially fitted, ensuring consistency in the treatment of bubble deformation.

3. Modeling

The theoretical model is derived from energy conservation principles by balancing pressure losses in the reactor, similar to previous studies [34,35,38].The pressure balance is

$$\Delta P_R = \Delta P_F + \Delta P_M + \Delta P_A + \Delta P_\varepsilon, \# \tag{3}$$

where ΔP_R represents the loss of pressure in the riser due to the presence of the gaseous phase, ΔP_F the loss of pressure due to friction, ΔP_M the minor pressure losses (geometrical details, such as bends and pipe elbows), and ΔP_a refers to the pressure loss in the riser owing to the acceleration of the liquid phase. Term ΔP_ε is newly introduced. It is associated with pressure losses due to turbulent dissipation in bubble wakes.

In the riser, the flow friction losses were calculated using a two-phase modeling approach, while single-phase modeling was employed in the downcomer, where no gaseous phase was present. This restricts the model's applicability to operating modes when gas is not recirculated into the downcomer. However, this does not restrict the implementation of gas recirculation in the model. The density difference between the two-phase mixture in the riser and the liquid in the downcomer represents the driving force of the reactor. The liquid recirculation velocity reaches a constant value when the pressure loss due to the gaseous phase in the riser equals the sum of the flow pressure losses. Considering the complex two-phase flow phenomena, the only parameter of interest is the gas holdup in the riser.

We assume all two-phase phenomena in a riser can be simplified using the homogeneous flow model with a simple additional pressure-loss term originating in the turbulent dissipation in bubble wakes. The additional term can be fitted experimentally or calculated theoretically using a specific flow-regime model, as shown in this paper.

3.1. The homogeneous flow model

The general assumption of the homogeneous flow model (HFM) is that the two-phase flow is well mixed and that the gas phase velocity w_L is equal to the liquid phase velocity w_G. Gas holdup α is written in terms of the mixture quality x as

$$\left.\begin{aligned} \alpha &= \frac{x}{x + (1-x)\frac{\rho_G}{\rho_L}}, \\ x &= \frac{\rho_G j_G}{\rho_G j_G + \rho_L j_L}, \end{aligned}\right\} \# \tag{4}$$

where $j_k = Q_k/A$ is the superficial velocity of the k-th phase (L liquid and G gas), Q is volumetric flow rate, and A is the conduit cross-sectional area.

Pressure loss in the riser is modeled simply as the hydrostatic pressure difference weighted by the gas holdup

$$\Delta P_R = \alpha(\rho_L - \rho_G)gH. \# \tag{5}$$

Pressure drop due to friction $\Delta P_F = \Delta P_{F,R} + \Delta P_{F,DC}$ is composed of the pressure drop in the riser $\Delta P_{F,R}$, which is calculated using a two-phase model and downcomer $\Delta P_{F,DC}$, for which a single-phase approach is used:

$$\Delta P_{F,R} = \frac{2H}{D\rho_m} f_m \dot{m}''^2 = \frac{2H}{D\rho_m} f_m (\rho_1 j_1 + \rho_2 j_2)^2, \# \tag{6}$$

$$\Delta P_{F,DC} = \frac{2H}{D} f_L \rho_L j_L^2, \# \tag{7}$$

where D is the diameter of the column and f_k is the Fanning friction factor of k-th phase. In Eq. (6) mixture density $\rho_m = \alpha\rho_G + (1-\alpha)\rho_L$ and absolute mass flux $\dot{m}'' = \rho_1 j_1 + \rho_2 j_2$ are used to account for both phases.

To determine the mixture Fanning friction factor f_m, the mixture Reynolds number $\mathrm{Re}_m = \dot{m}'' D/\mu_m A$ is used, where the mixture viscosity is $\mu_m = \alpha\mu_G + (1-\alpha)\mu_L$. Friction pressure losses in the separator and the reactor base are neglected due to the relative shortness of these sections.

Minor pressure losses are evaluated in three sections: the riser outflow $\Delta P_{M,R}$, the downcomer inflow $\Delta P_{M,DC}$ and the base $\Delta P_{M,B}$, so that $\Delta P_M = \Delta P_{M,R} + \Delta P_{M,DC} + \Delta P_{M,B}$. They are calculated based on the minor loss coefficients K, which are widely documented in the literature. See for example [41].

$$\left.\begin{aligned} \Delta P_{M,R} &= 0.5\rho_m K_R j_L^2, \\ \Delta P_{M,DC} &= 0.5\rho_L K_{DC} j_L^2, \\ \Delta P_{M,B} &= 0.5\rho_L K_B j_L^2, \end{aligned}\right\}\# \tag{8}$$

where K_R, K_{DC} and K_B are 1, 2.2, and 0.2 for the reactor used in the study, respectively.

Pressure drop due to acceleration of the liquid phase ΔP_A is calculated in terms of energy conservation for the liquid phase in the region of gas injection. Before the injection of gas, the liquid velocity is w_L, after injection, it increases to w_L' to accommodate a smaller flow cross-section. Therefore,

$$\Delta P_A = 0.5\rho_L\left(w_L'^2 - w_L^2\right), \# \tag{9}$$

where the notation is the same as for the following set of equations: A_k and w_k are the cross-sectional area of the channel filled by phase k and the absolute or the phase velocity of the phase k, respectively. An apostrophe denotes the section after the injection of the gas. From the conservation of mass, $w_L A_L = w_L' A_L'$, where $A_L' = (1-\alpha)A$, the velocity of the liquid phase after gas injection can be calculated as $w_L' = w_L(1-\alpha)^{-1}$. Since the volume before the gas injection is presumed to be filled by the liquid phase, the phase velocity w_L can be substituted with the liquid superficial velocity j_L. Pressure drop due to the acceleration is then

$$\Delta P_A = 0.5\rho_L j_L^2\left((1-\alpha)^{-2} - 1\right).\# \tag{10}$$

Until now, the treatment of two-phase flow phenomena in the riser has been avoided. Using the homogeneous flow assumption, the fluid is described as an isotropic mixture without interfacial phenomena. However, when the entire reactor is treated as a pressure-balanced system, the turbulent energy losses generated in the wake of the bubbles cannot be neglected.

A central novelty of the present paper is introducing an additional term that covers such pressure losses in the flow while maintaining the simplicity of the homogeneous approach. Here, we propose a pressure loss term, which draws its analogy from the minor pressure loss term. It is calculated as

$$\Delta P_\varepsilon = 0.5\rho_L \varepsilon j_L^n, \# \tag{11}$$

with ε representing the newly proposed reactor dissipation parameter, which we presume is constant for a single reactor geometry. The scaling of the dissipation pressure loss with the liquid superficial velocity is achieved by the free parameter n, which we calculate in the following section.

Although minor losses arise from localized geometric disruptions (e.g., bends, valves) and our term accounts for distributed turbulent dissipation in bubble wakes, both contribute to additional resistance in the system. We, therefore, propose a pressure loss term analogous to minor losses. This mathematical similarity allows for a straightforward implementation while retaining physical relevance. Additionally, the two free parameters in Eq. (11) enable empirical fitting, making the model easily adaptable when the theoretical approach is not feasible.

3.2. Determining the free parameter n

Parameter n points to the intensity of the turbulent mixing in the wake of the bubbles regarding the gas holdup and corresponding induced liquid flow rate. We can either fit the model to experimental data or try to deduce it theoretically to determine it. As such, the model can be derived as an empirical or a theoretical model.

In this section, we establish a theoretical model by connecting the turbulent wakes to the drag of the gaseous structures. We are interested in the drag coefficient because we can expect that the wake region, and thus the induced turbulence, scales with the drag imposed on the particles. We can use this assumption to link the free parameter to a physical quantity and determine an appropriate scaling law.

Based on the structure of the observed dispersed phase in airlift reactors, we can characterize the majority of gas bubbles with the *distorted fluid-particle regime* [42,43]. In this regime, a vortex system develops behind the bubble, and the drag force on the bubble is primarily determined by the eddies generated by the flow separation, which is approximately proportional to the inertial force. The strong contribution of the turbulent eddies in the wake region leads to increased drag of the bubbles owing to the presence of other particles and $C_{D\infty}$ becomes unrelated to the velocity and the viscosity of the carrier phase and depends only on the radius r_d [43],

$$\left.\begin{aligned} C_D &= C_{D\infty}\left(\frac{1+17.67(1-\alpha)^{1.3}}{18.67(1-\alpha)^{1.5}}\right)^2, \\ C_{D\infty} &= \frac{4}{3} r_d \sqrt{\frac{g\Delta\rho}{\sigma}}. \end{aligned}\right\}\# \tag{12}$$

Eq. (12) approximates the drag coefficient concerning the gas holdup and the average bubble diameter for distorted bubbles. This is particularly interesting because we observed such fluid structures in every regime in the reactor.

Limiting the flow in a confined space leads to larger gas structures, or slugs, at higher gas holdup values, characteristic of the *slug-flow regime*. The analogy between drag and induced turbulence ends here. The geometry of the slugs completely transforms the flow field around them, forming a thin liquid film on the pipe wall and entrapping smaller bubbles in their wakes. At the bubble-to-slug flow transition, the drag coefficient is more significant for the slug flow, but it exhibits a negative trend with increased gas holdup [42]. This should not discourage drag to turbulence scaling assumption because even at the highest gas flow rates, the flow starts as a distorted fluid-particle regime and only converges to the slug flow around the middle of the riser. Even at the top of the riser, where slugs are fully formed, an intermediate section with the same distorted fluid-particle regime is observed between the slugs.

To summarize, we are anticipating a relationship between the drag coefficient C_D of the gaseous structures and the reactor gas holdup α, which is by itself closely related to the induced liquid superficial velocity j_L. Such a relationship, $C_D \propto j_L^n$, should yield a scaling parameter n, connecting the dissipation pressure losses to an underlying physical principle, which is, in the first approximation, based on the imposed drag. Experimental investigation of the proposed solution is provided in Sec. 4.2.

3.3. Determining the reactor dissipation parameter ε

Similarly to n, the reactor dissipation parameter must be determined either empirically or theoretically. Based on our findings (see Sec. 4), we propose the universality of ε for a constant ratio between the riser and downcomer cross-section. This agrees with the rationale behind the approach because the riser's cross-sectional area influences the bubbles' size and arrangement, and the downcomer's cross-sectional area influences the liquid superficial velocity and, subsequently, the gas–liquid interface dynamics.

To assess the reactor dissipation parameter, we suggest that the $j_L(\alpha)$ curve predicted by the HFM is compared to the same curve of a flow-regime-specific model in the region of interest, from which the ε can then be calculated via the least squares method.

A simple separated flow model (SFM) is proposed, which again follows from Eq. (3). The last pressure term ΔP_ε is absent here since the interface phenomena are already captured in the friction terms by the Lockhart-Martinelli [44] and Chisholm [45] correlations. Equations derived in Sec. 3.1 remain primarily unmodified. Firstly, the calculation of the gas holdup changes according to [46],

$$\alpha = \frac{1}{1 + c\left(\frac{1-x}{x}\right)^{q}\left(\frac{\rho_G}{\rho_L}\right)^{r}\left(\frac{\mu_L}{\mu_G}\right)^{s}}\# \tag{13}$$

where the empirical constants are $c = 0.28$, $q = 0.64$, $r = 0.36$ and $s = 0.07$ [45]. The correlation proposed initially in [44] can also be used. However, it tends to overpredict the mass flow rate.

Secondly, the pressure drop in the riser is augmented following the Lockhart–Martinelli model by the pressure drop multiplier Φ, so

$$\Delta P_{F,R} = \Phi_L^2 \Delta P_L = \Phi_L^2 \frac{2H}{D} f_L \rho_L j_L^2, \# \tag{14}$$

where ΔP_L is the friction pressure drop of the liquid phase, and the pressure drop multiplier Φ is calculated via the Martinelli parameter X as

$$\left.\begin{aligned} \Phi_L^2 &= 1 + \frac{C}{X} + \frac{1}{X^2}, \\ X &= \sqrt{\frac{f_L \rho_L}{f_G \rho_G}}\left(\frac{j_L}{j_G}\right)^2, \end{aligned}\right\}\# \tag{15}$$

where C is a dimensionless constant proposed by [44] (see Table 1).

Lastly, the riser's minor pressure loss is also augmented by the separated flow correction,

$$\Delta P_{M,R} = 0.5 \Phi_L \rho_L K_R j_L^2 .\# \tag{16}$$

To summarize, we can model the induced liquid velocity in the reactor with the SFM, which should be in good agreement with the experimental data in the separated flow regime. We can further model the induced velocity with the HFM, which will generally differ from the SFM. Since the two should coincide in the separated flow regime, if the augmented HFM truly captures multiple regimes, we can back-calculate the corresponding ε value. This is demonstrated in Sec. 4.

4. Results and discussion

Fig. 3 shows the experimental results for the gas holdup and liquid superficial velocity as a function of the superficial gas velocity. The data points represent average measured values with maximum and minimum deviations. The reactor operates over a relatively broad range of gas holdup values up to 0.2. This broad range results in different flow regimes and their intermediate modes, influencing pressure signal measurements. They result in higher uncertainty in the gas holdup values, especially at the bubbly to-slug transition.

Table 1
Value of C, based on the liquid and gas phases. Viscous limit is $\mathrm{Re}_k < 2000$ for phase k. [46].

Liquid	Gas	C
viscous	viscous	5
turbulent	viscous	10
viscous	turbulent	12
turbulent	turbulent	20

4.1. Flow regime identification

As described in the previous section, the flow was imaged at three locations along the riser to capture the spatial development of the regimes. Spectral analysis was used to obtain the PSDF of the pressure fluctuations, which was used to further distinguish between the regimes. Fig. 4a-c show three typical PSDFs and their corresponding flow regimes. Fig. 4d demonstrates the relationship between the dominant peak frequency and the gas superficial velocity.

Structures such as bubbles and slugs influence the flow and pressure fields in their vicinity through their geometry, frequency, and spatial evolution. Thus, typical PSDF shapes and frequency bands were obtained for particular regimes and structures. Our reactor features two frequency bands with an intermediate section (Fig. 4b) where a transition occurs between the two flow regimes. The PSDF exhibits a dominant high-frequency band in the homogeneous regime with peaks between 10 and 25 Hz (Fig. 4a). The amplitude of this band remained constant at higher gas holdup values. This can be attributed to lower amplitudes at higher frequencies associated with smaller structures, such as bubbles, which are constantly present in the riser. In the heterogeneous or slug-like regimes, the PSDF exhibited a dominant low-frequency band with peaks between 4 and 8 Hz (Fig. 4c).

The amplitude of the peaks in the low-frequency band increases constantly with increasing gas holdup and becomes dominant when slugs start to form in the riser. Their high amplitudes at low frequencies can be associated with larger structures like slugs. Fig. 4d shows that the predominant frequencies decreased as the superficial gas velocity increased.

The transition between flow regimes was analyzed using both global and local approaches. Globally, pressure signal decomposition (Fig. 4d) identified characteristic frequency shifts associated with different flow patterns, while locally, high-speed footage captured the vertical evolution of bubble structures along the riser. Across all conditions, the dominant two-phase structure observed was the distorted fluid-particle regime [42], which persisted throughout the riser height except at very high gas flow rates, where slug flow developed near the top. Unlike regime-specific models, the proposed HFM inherently accounts for these transitions without requiring separate flow regime classifications. This is supported by experimental data (Fig. 7, bottom), demonstrating the model's ability to predict induced liquid velocity across different flow conditions consistently.

4.2. Calculating the free parameter n

As described in Sec. 3.2, we are calculating the free parameter n from the relationship between the drag coefficient and gas holdup. Upon spectral analysis and confirmation via visual observation via high-speed footage, we concluded that the distorted fluid-particle regime was present over the entire gas holdup. Therefore, at higher gas holdups, where higher energy dissipation rates are expected due to the turbulent nature of the flow, larger bubble radiuses are also found, which result in higher drag coefficients.

Average bubble chord length varies vertically in the riser, with higher locations producing longer chords and lower locations producing shorter ones, influencing the drag coefficient. However, if we assume a uniform bubble chord length distribution and measure it only in the middle section, as done in our study, the differences between the top and bottom cancel out to some extent. Modeling the distribution effects in detail would increase model complexity, such as adding pressure loss terms for specific flow patterns (see Camarasa et al.). [35]), in contrast to our aim of reducing this complexity. This choice, therefore, provides a representative estimate of bubble dynamics without being biased by initial injection effects near the sparger or coalescence-dominated regions near the top. The model's performance against various experimental datasets supports our simplification.

Nine sets of similar bubble sizes (see Sec. 3.2) were thus analyzed,

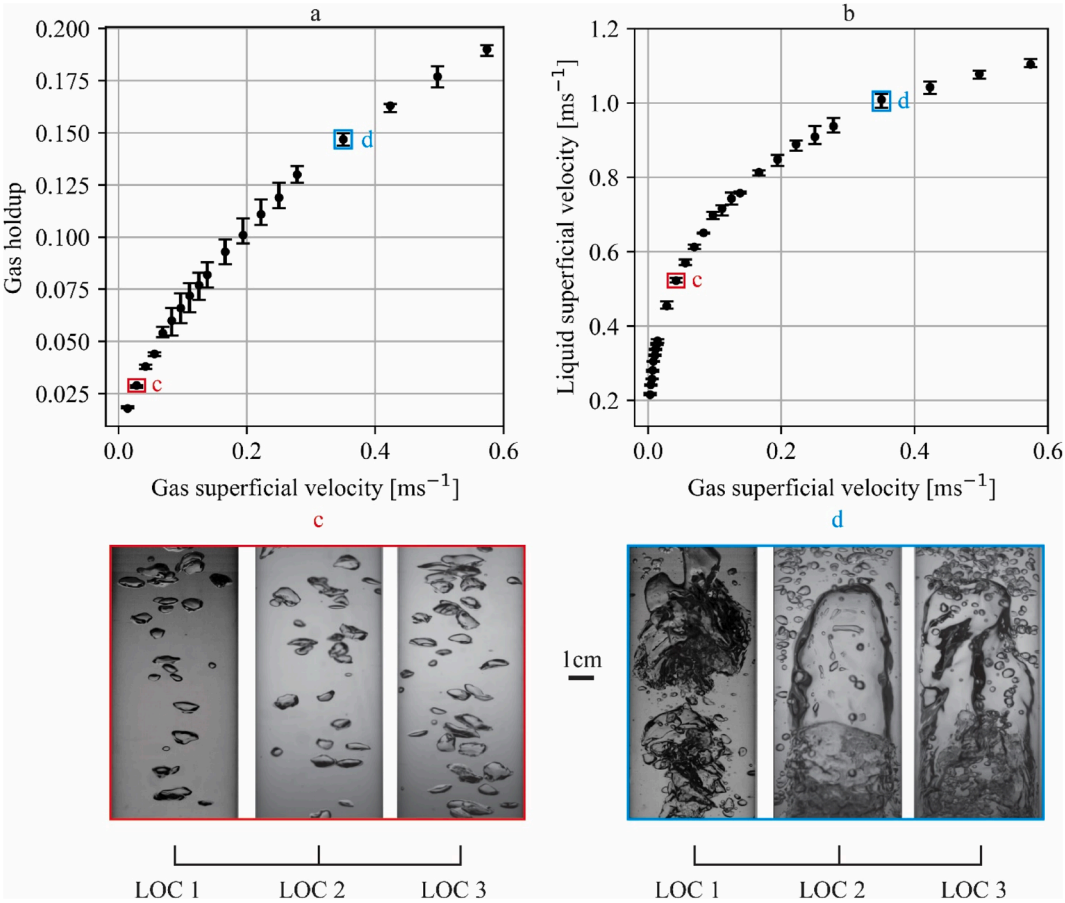

Fig. 3. Gas holdup (a) and liquid superficial velocity (b) as a function of gas superficial velocity. Bubbly ($\alpha = 0.029$) and slug ($\alpha = 0.147$) flow regimes are showcased in c and d, respectively. Locations LOC1-3 correspond to the filming location described in Sec. 2.1.

and the average dimensionless radius of each set was calculated using Eq. (12). The relationship between r_d^* and gas holdup is shown in Fig. 5a, along with some typical structures. The corresponding drag coefficient for each set is shown in Fig. 5b, normalized to the highest value.

It is found that C_D scales with a power of 1.5 concerning the gas holdup. Considering the gas holdup scales roughly linearly with the liquid superficial velocity ($R^2 = 0.961$), we can assume $C_D \propto \alpha^{1.5} \propto j_L^{1.5}$, following the discussion in Sec. 3.2. Pressure loss due to the dissipation ΔP_ε is thus

$$\Delta P_\varepsilon = 0.5 \rho_L \varepsilon j_L^{1.5}.\# \tag{17}$$

Although derived from the experimental analysis of a single specific ELALR, the power correlation should hold for other reactors with similar geometry, as shown in Sec. 4.6. For other reactor types, like ILALR, the free parameter n should be recalculated in the manner shown here or fitted empirically.

4.3. Calculating the reactor dissipation parameterε

Following the discussion in Sec. 3.3, the HFM model prediction of $j_L(j_G)$ is plotted next to the prediction of the SFM in Fig. 6. In Fig. 6a, the dissipation pressure loss term of the HFM is zero ($\varepsilon = 0$), and we see that the model overpredicts the induced liquid velocity at higher gas superficial velocities compared to the SFM in the region where separated flow regime is observed (Fig. 4d). This increase in induced liquid velocity is the direct result of underpredicting pressure losses in the reactor since the system's energy is conserved. To obtain the correct value of ε, the HFM and SFM should match closely in the separated flow region. Fig. 6b shows both models, with $\varepsilon = 3$ for the HFM. Models show strong agreement in the separated flow regime, whereas, in the homogeneous flow region, the SFM overpredicts the induced liquid velocity compared to HFM.

We expect the reactor dissipation parameter to differ for different reactor geometries, especially the riser to downcomer cross-sectional area. Still, it should be in a similar value range for reactors of similar geometry. The dependence of ε on reactor geometry is shown in Sec. 4.6.

4.4. Homogeneous flow model performance

The homogeneous flow model with the energy dissipation pressure loss ($\varepsilon = 3$) agrees with the experimental values over the tested gas holdup region. Without the newly proposed term ($\varepsilon = 0$), the model overpredicts the induced velocity over the entire experimental gas holdup since lower energy dissipation is predicted. Both instances are presented in Fig. 7.

Our set of measurements shown in closeup a and b of Fig. 7 was further compared with a recent analytical model [37,38] in Fig. 8. The presented range of superficial velocities was specifically selected to be in the same range as the gas superficial velocities reported by [38]. Their pressure balance model was developed specifically for low gas flow rates and simple geometries, where two-phase flow phenomena are omitted apart from the term ΔP_R and is thus even more straightforward than the HFM reported here. Here, we show that the model's accuracy can be significantly improved with a minimal increase in complexity. Nonetheless, it must be stated that the accuracy of the [38] model is exceptional if one considers just how simplistic it is.

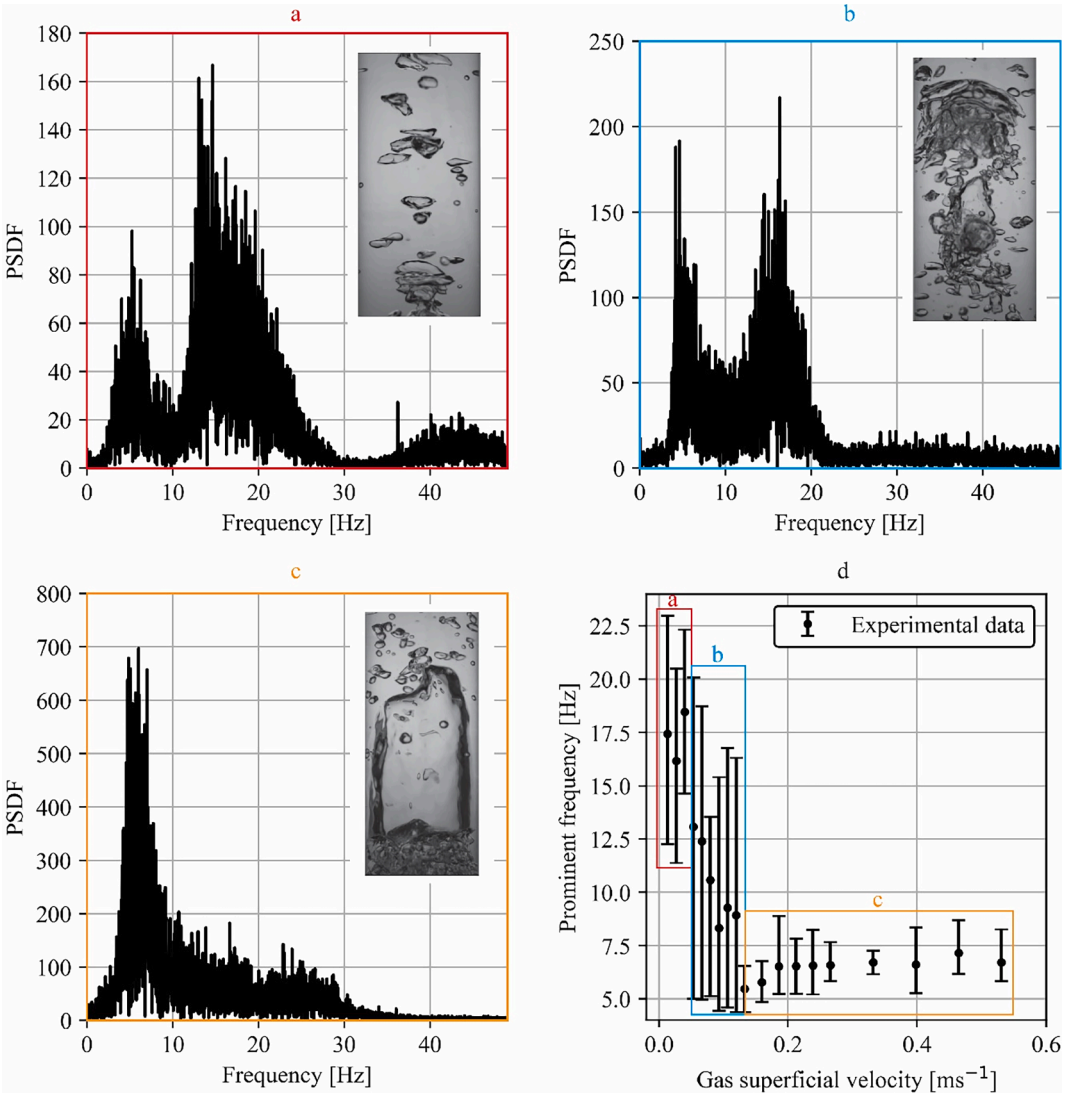

Fig. 4. Spectral analysis of the pressure signal. Details a-c display three typical PSDF forms. homogeneous, transitional, and heterogeneous flow. All three images were captured at 1024 mm above the sparger. The data points in d are represented by the average measured values with maximum and minimum deviations.

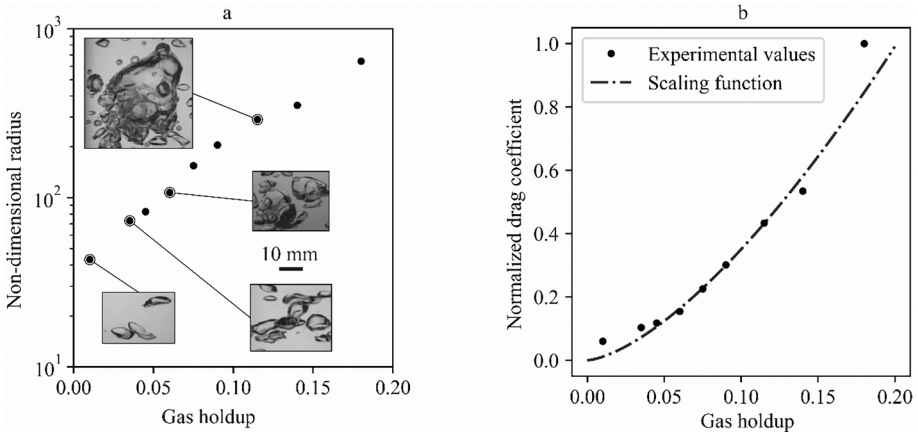

Fig. 5. Non-dimensional radius (a) and normalized drag coefficient (b) in relation to gas holdup. Nine sets of similar bubble size are plotted. The equation for the scaling function is $y = 182x^{1.5}$ with $R^2 = 0.97$.

4.5. Separated flow model performance

Fig. 9 shows excellent agreement between the experimental values and SFM in the high gas holdup region, where the riser flow was separated. The SFM's 10 percent error margin persists in the transition region of the two-phase flow. The fit in the bubbly flow region, where the

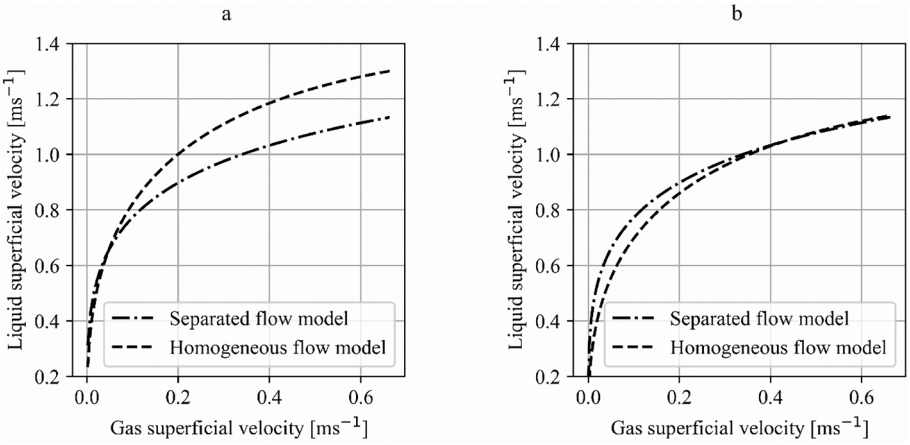

Fig. 6. Comparison of HFM and SFM in the superficial velocity space. $\varepsilon = 0$ in (a) and $\varepsilon = 3$ in (b).

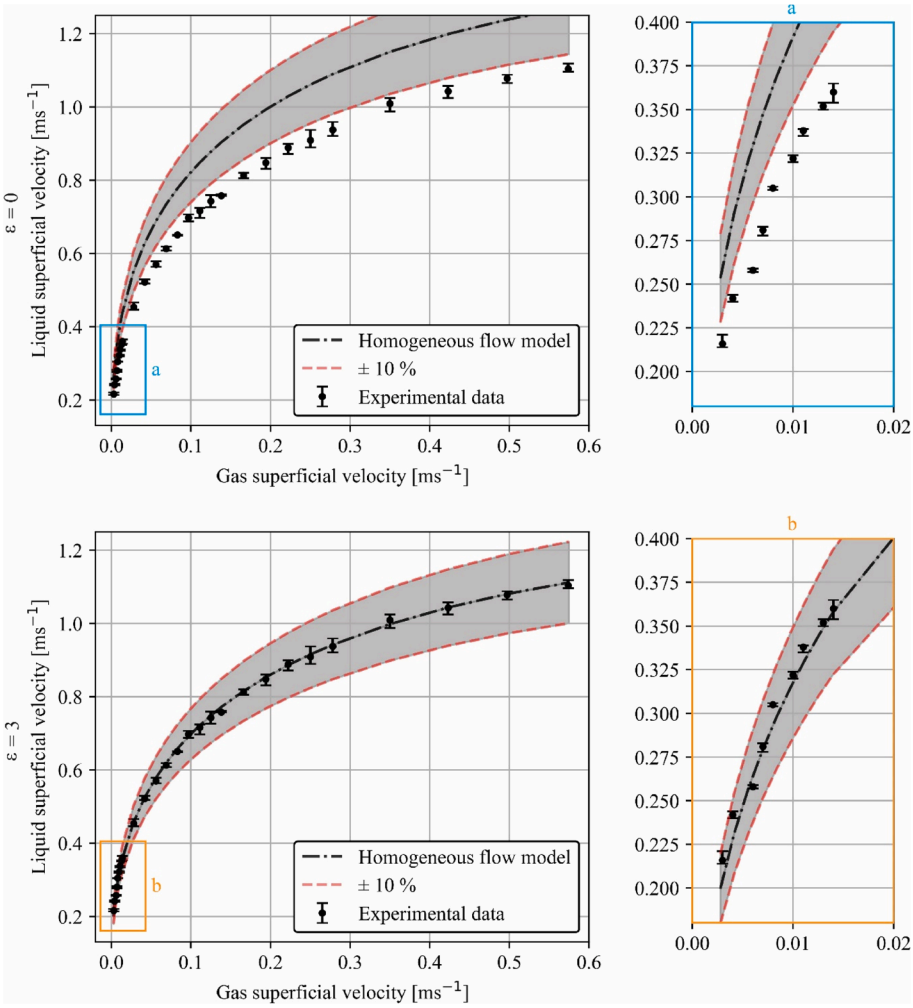

Fig. 7. Homogeneous flow model performance with our experimental data with $\varepsilon = 0$ (top) and $\varepsilon = 3$ (bottom). Details a and b show the closeup at the lowest gas superficial velocities.

flow homogeneity is expected, is reduced by as much as 50 percent. This is anticipated because the model assumes a slip between the phases and is not intended for modeling in that low gas holdup region.

4.6. *Dependence of ε on reactor geometry*

The upgraded homogeneous flow model was tested using the experimental data obtained in [38]. Because the HFM depends on known minor pressure loss coefficients, the exact geometrical parameters of the reactor must be known. We applied an upgraded HFM to five

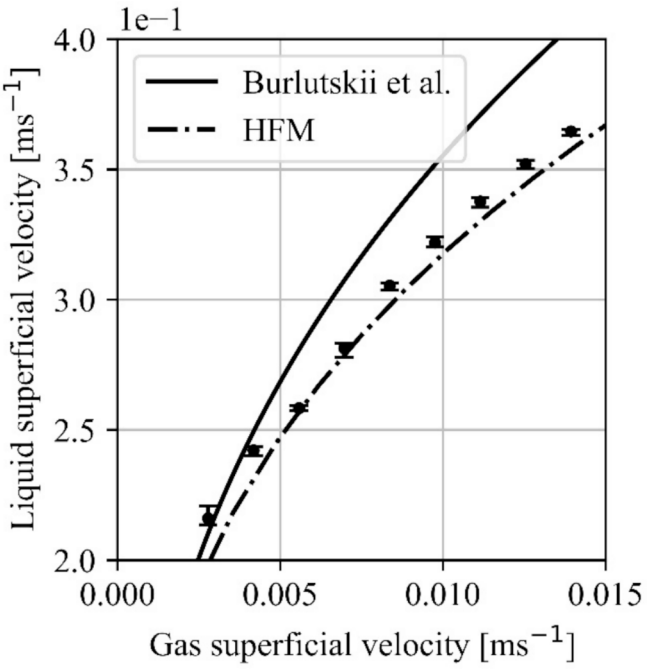

Fig. 8. HFM compared to the [38] model at low gas superficial velocities. The HFM maintains the experimental trend at increased gas superficial velocities, while the [38] model veers off owing to the simplistic theoretical approach.

experimental sets from [38]. Their experiments featured square ducts with a simple base-and-separator design. Table 2 lists the geometrical parameters and calculated ε values required to obtain the best HFM performance.

The study reported by Burlutskii et al. [38] was executed at very low gas superficial velocities ($j_g < 0.015 \mathrm{ms}^{-1}$), indicating that no flow regime transition was observed. Moreover, their experimental design succumbed to recirculating the gas bubbles in the downcomer at certain riser-to-downcomer duct-side ratios. This made predictions using the SFM counterintuitive because whether the reactor can operate in the separated flow regime without downcomer gas recirculation is unknown. Therefore, the HFM was first evaluated in a riser-to-downcomer area ratio of 1 and an $\varepsilon = 3$, corresponding to our experimental reactor. The HFM predicts the experimental values well, as shown in Fig. 10.

The HFM was then compared with other experimental data with riser-to-downcomer duct-side ratios not equal to one. It was found that ε depends on the riser-to-downcomer area ratio. It must be noted here that the ε was not calculated from the SFM since SFM was not used in this study. The ε was calculated based on a fit between the experimental and theoretical data.

As shown in Fig. 10, the HFM achieves an outstanding experimental trend, and the ε assumes physically logical values for sets 1–3. Sets 4 and 5 were characterized by low and extremely low superficial velocities. It seems that the model underpredicts the pressure loss for such low superficial velocities in this specific reactor and thus requires very high ε values. The HFM should be viewed more as a fitted engineering model than a theoretical model for such sets.

4.7. Investigation of individual pressure loss contribution

To provide further insight into the workings of ELALRs, Eq. (3) is decomposed into singular terms, and their contribution is shown in Fig. 11 (our reactor geometry is used). Here, the pressure losses are normalized to the highest value (ΔP_R at highest gas holdup) and are plotted for the whole observed gas superficial velocity region. Note that the pressure loss in the riser equals the sum of all other contributions.

At low gas superficial velocities, where homogeneous flow is observed, the dissipation and minor pressure losses represent the highest fraction in the reactor. After the transition to the separated flow, the highest energy losses are induced by the geometrical obstructions in the flow. The pressure loss due to the acceleration of the carrier phase is negligible at lower gas holdup values but rises to a considerable fraction in the separated flow regime. Such observations agree with the reactor characteristics (see Fig. 3b) since the induced liquid velocity has a sharp velocity gradient at low gas holdup values.

5. Conclusion

The study introduces an improved modeling approach for predicting the liquid phase's recirculating velocity in external loop airlift reactors. The model is based on the homogeneous flow assumption and presents a

Table 2
Geometrical and model parameters [38].

Set	Riser duct side [m]	Downcomer duct side [m]	Height [m]	ε
1	0.025	0.1	2	0.1
2	0.05	0.1	2	1.3
3	0.1	0.1	2	3
4	0.1	0.05	2	40
5	0.1	0.025	2	1700

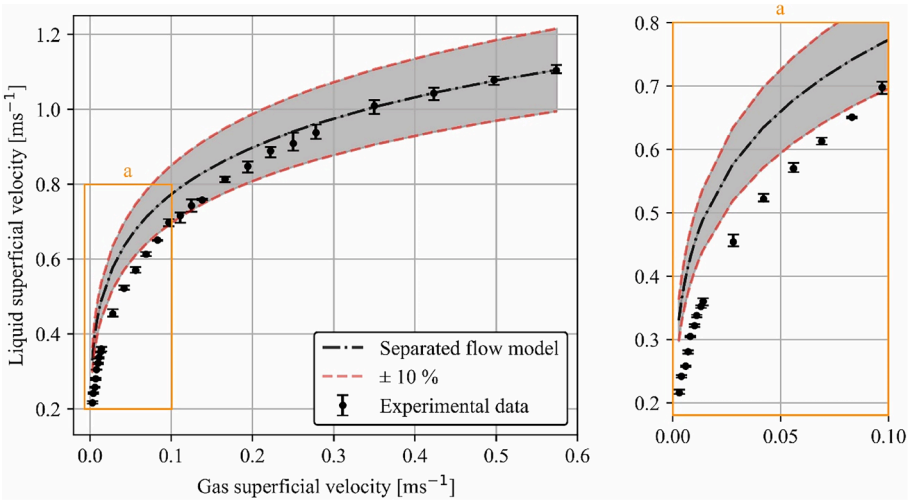

Fig. 9. Separated flow model performance. Detail a shows a closeup at the lowest gas superficial velocities.

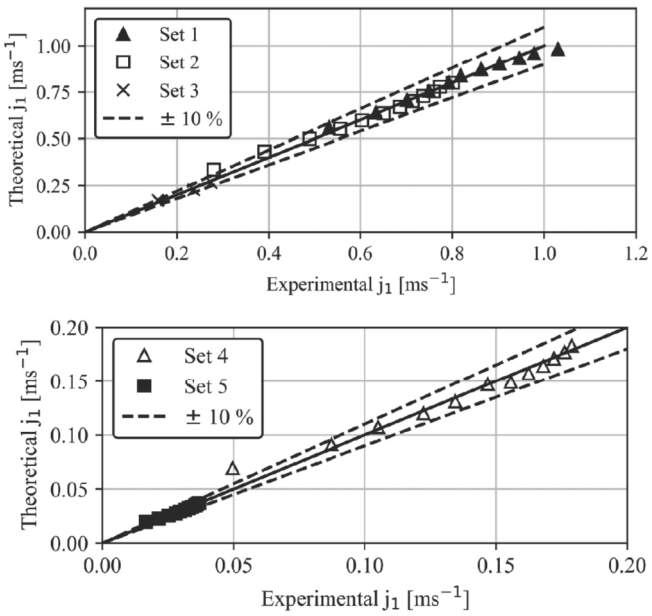

Fig. 10. HFM performance on [38] experimental data. The riser to downcomer duct side ratio is: Set 1: 0.25, Set 2. 0.5, Set 3: 1, Set 4: 2 and Set 5: 4.

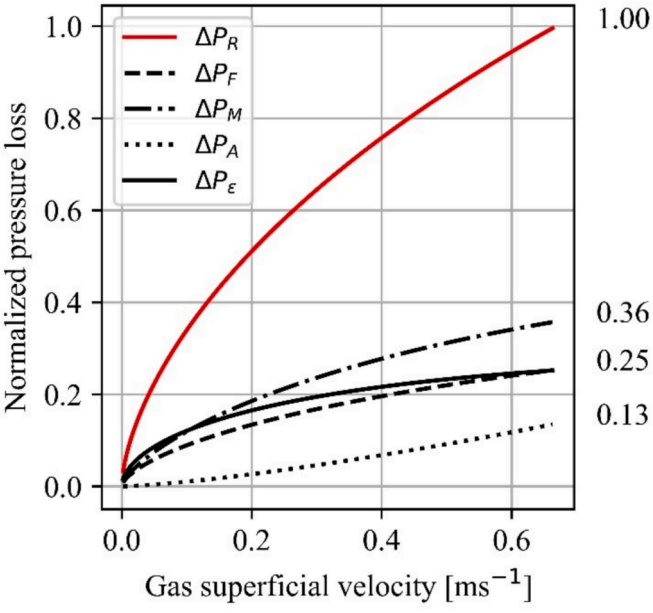

Fig. 11. Pressure loss term contribution for our reactor, see Eq. (3). Pressure loss is normalized to the highest value observed.

novel pressure loss term originating from the energy dissipation in wakes behind gaseous structures. The proposed model was tested with our experimental data in the wide range of gas and liquid superficial velocities, covering all flow regimes typically encountered in airlift reactors. Furthermore, the model was also tested against various reactor geometries from the literature [38]. In addition, a second model was developed, which assumed a separated flow. Experimental data and the predictions of both models were in excellent agreement.

The novel reactor dissipation parameter ε introduced in the study can be theoretically predicted or fitted experimentally. Both methods are presented in the paper. It is shown to be dependent on the cross-sectional ratio between the riser and the downcomer and was found to be constant for similar reactor geometries. In both our reactor (circular ducts) and the reactor from the literature [38] (rectangular ducts), with the same riser to downcomer cross-sectional ratio of 1, the reactor dissipation constant ε was equal to 3.

To determine the free parameter n, which points to the intensity of the turbulent mixing in the wake of the bubbles concerning the gas holdup, we proposed a first-order approximation based on the connection between the drag coefficient and energy dissipation in the bubble wake. We calculated a correlation $C_D \propto \alpha^{1.5} \propto j_L^{1.5}$ from the bubble chord visual measurements at different gas holdup values. We found it to be universally constant for all modeled experimental data.

Analysis of the terms of pressure loss indicates that minor pressure losses are the most significant contributors to the overall pressure drop in the reactor. Optimizing reactor geometry (e.g., bends, sparger, inflow, and outflow design) enhances the reactor's energy efficiency.

Predicting liquid circulation and gas distribution with high accuracy is critical for optimizing convective heat transfer, turbulence modulation, and phase change processes. These insights are particularly relevant for the design of energy-efficient heat exchangers, industrial cooling systems, and boiling heat transfer applications. The model's simplicity makes it readily integrable into higher-fidelity heat and mass transfer simulations, enabling more detailed studies of bubble-induced convective enhancement. Additionally, its framework provides a foundation for future research on hybrid reactor systems, where multiphase flow behavior is coupled with heat and mass transfer in chemically reactive environments.

The models derived in this paper are limited to situations where the gas does not recirculate into the downcomer. While tiny bubbles can contribute to overall gas holdup, our measurements focused on the riser, and no recirculation was observed under the large spectra of tested conditions. The maximum gas superficial velocity was deliberately kept below the threshold for recirculation, and the downcomer geometry minimizes gas entrainment by positioning the gas discharge well away from its entrance. Thus, riser measurements are a reliable representation of global gas holdup, though downcomer contributions may become significant at higher-than-reported gas flow rates. These cases can be generalized by applying an appropriate two-phase flow treatment in the downcomer. The application of the HFM and the SFM models is principally not limited to ALR but can be extended to other airlift systems. The simplicity of the HFM makes it especially useful for integration in coupled models of higher complexity, including, but not limited to, heat and mass transfer models.

Declaration of competing interest

The authors declare that they have no known competing financial interests or personal relationships that could have appeared to influence the work reported in this paper.

Acknowledgements

The authors would like to acknowledge Matic Cotič for his help in setting up the experiment. Financial support was provided by the Slovenian Research and Innovation Agency under programme group No. P2-0162.

Appendix A:. Measurement uncertainty

Liquid velocity

Flowmeter from Georg Fischer (U1000 V2) was used with accuracy of ± 3 % (measured value) and repeatability of ± 0.5 % (measured value). The expanded liquid velocity measurement uncertainty (95 % confidence level) is

$$U(v_l) = 2 \cdot u(v_l) = 2 \cdot \frac{0.03 \cdot v_l + 0.005 \cdot v_l}{\sqrt{3}} \mathrm{m/s}. \# \tag{A1}$$

For the lowest and highest measured liquid velocities v_j in the downcomer, 0.2 and 1.1 m/s, the expanded measurement uncertainty is 0.008 m/s (4 %) and 0.044 m/s (4 %), respectively.

Pressure

Differential pressure gauge from Greisinger (GDH 07 AN), full scale 0.0–199.9 mbar, was used with accuracy of ± 0.1 mbar and ± 0.2 % full scale, with additional temperature influence of ± 0.4 % full scale. The expanded pressure difference measurement uncertainty (95 % confidence level) is

$$U(\Delta P) = 2 \cdot u(\Delta P) = 2 \cdot \frac{0.1 + 0.002 \cdot 199.9 + 0.004 \cdot 199.9}{\sqrt{3}} = 1.5 \mathrm{mbar}. \# \tag{A2}$$

For the lowest and highest measured pressure differences in the riser, 155 and 190 mbar, the expanded measurement uncertainty is 0.98 % and 0.79 %, respectively.

Gas velocity

Three rotameters from Honsberg were used to measure the gas flow rate, 0–5 L/h, 0–20 L/h, and 0–100 L/h range, all with an accuracy of ± 3 full scale. The superficial velocity was recovered by dividing the gas flow rate by the duct's cross-section. To ensure optimal measurement range, the 0–5 L/h rotameter was used in the gas superficial velocity range of 0–0.015 m/s, the 0–20 L/h rotameter was used in the range of 0.015–0.06 m/s and the 0–100 L/h rotameter was used in the range of 0.06–0.2 m/s. The corresponding expanded gas superficial velocity measurements uncertainties (95 % confidence level) are:

$$U\left(j_{g,0-5\mathrm{L/h}}\right) = 2 \cdot \frac{0.0005}{\sqrt{3}} = 0.00058 \mathrm{m/s}, \# \tag{A3}$$

$$U\left(j_{g,0-20\mathrm{L/h}}\right) = 2 \cdot \frac{0.002}{\sqrt{3}} = 0.0023 \mathrm{m/s}, \# \tag{A4}$$

$$U\left(j_{g,0-100\mathrm{L/h}}\right) = 2 \cdot \frac{0.009}{\sqrt{3}} = 0.01 \mathrm{m/s}. \# \tag{A5}$$

The highest expanded measurement uncertainty is at the rotameter switch values (5 and 20 L/h), which reaches 15 %, corresponding to the larger rotameter measuring at its lower range. The lowest expanded measurement uncertainty was 3.8 %, corresponding to rotameters measuring near the maxima of their range.

Data availability

Data will be made available on request.

References

[1] S. Hosokawa, S. Fujimoto, A. Tomiyama, Gaslift pump making use of phase change of working fluid, *Appl. Therm. Eng.* 103 (2016) 1119–1125, https://doi.org/10.1016/j.applthermaleng.2016.05.010.

[2] T. Zhang, C. Wei, C. Feng, Y. Ren, H. Wu, S. Preis, Advances in characteristics analysis, measurement methods and modelling of flow dynamics in airlift reactors, *Chem. Eng. Process. - Process Intesif.* 144 (2019) 107633, https://doi.org/10.1016/j.cep.2019.107633.

[3] W.R. Kessler, M.K. Popović, C.W. Robinson, Xanthan production in an external-circulation-loop airlift fermenter, *Can J Chem Eng* 71 (1) (1993) 101–106, https://doi.org/10.1002/cjce:5450710114.

[4] B. Srinivasulu, R.S. Prakasham, A. Jetty, S. Srinivas, P. Ellaiah, S.V. Ramakrishna, Neomycin production with free and immobilized cells of Streptomyces marinensis in an airlift reactor, *Process Biochem.* 38 (4) (2002) 593–598, https://doi.org/10.1016/S0032-9592(02)00182-6.

[5] S. Sun, C. Liu, W. Wei, X. Bao, Hydrodynamics of an annulus airlift reactor, *Powder Technol.* 162 (3) (2006) 201–207, https://doi.org/10.1016/j.powtec.2005.08.025.

[6] S.M. Mousavi, S. Yaghmaei, M. Vossoughi, A. Jafari, S.A. Hoseini, Comparison of bioleaching ability of two native mesophilic and thermophilic bacteria on copper recovery from chalcopyrite concentrate in an airlift bioreactor, *Hydrometall.* 80 (1–2) (2005) 139–144, https://doi.org/10.1016/j.hydromet.2005.08.001.

[7] D. Fang, L.-X. Zhou, Enhanced Cr bioleaching efficiency from tannery sludge with coinoculation of Acidithiobacillus thiooxidans TS6 and Brettanomyces B65 in an air-lift reactor, *Chemosphere* 69 (2) (2007) 303–310, https://doi.org/10.1016/j.chemosphere.2007.03.059.

[8] C. Nicolella, Wastewater treatment with particulate biofilm reactors, *J. Biotechnol.* 80 (1) (2000) 1–33, https://doi.org/10.1016/S0168-1656(00)00229-7.

[9] L. Xianling, W. Jianping, Y. Qing, Z. Xueming, The pilot study for oil refinery wastewater treatment using a gas–liquid–solid three-phase flow airlift loop bioreactor, *Biochem. Eng. J.* 27 (1) (2005) 40–44, https://doi.org/10.1016/j.bej.2005.06.013.

[10] F. Hesse, M. Ebel, N. Konisch, R. Sterlinski, W. Kessler, R. Wagner, Comparison of a production process in a membrane-aerated stirred tank and up to 1000-L airlift bioreactors using BHK-21 cells and chemically defined protein-free medium, *Biotechnol. Prog.*, 19 (3) (2003) 833–843, https://doi.org/10.1021/bp0257630.

[11] W.S. Tan, G.C. Dai, W. Ye, J.P. Shen, Local flow behavior of the liquid phase in an airlift bioreactor for potential use in animal cell suspension cultures, *The Chemical Engineering Journal and the Biochemical Engineering Journal* 57 (3) (1995) B31–B36, https://doi.org/10.1016/0923-0467(94)06092-4.

[12] H.F. Svendsen, H.A. Jakobsen, R. Torvik, Local flow structures in internal loop and bubble column reactors, *Chem. Eng. Sci.* 47 (13–14) (1992) 3297–3304, https://doi.org/10.1016/0009-2509(92)85038-D.

[13] M.J. Barbosa, M. Janssen, N. Ham, J. Tramper, R.H. Wijffels, Microalgae cultivation in air-lift reactors: modeling biomass yield and growth rate as a function of mixing frequency, *Biotech & Bioengineering* 82 (2) (2003) 170–179, https://doi.org/10.1002/bit.10563.

[14] M. Blažej, J. Annus, J. Markoš, Comparison of gassing-out and pressure-step dynamic methods for kla measurement in an airlift reactor with internal loop, *Chem. Eng. Res. Des.* 82 (10) (2004) 1375–1382, https://doi.org/10.1205/cerd.82.10.1375.46737.
[15] D. Klembt, H. Meironke, A. Delgado, The heat and mass transfer of a fermenting multiphase flow using acoustic measurement technology and numerical methods, *Appl. Therm. Eng.* 199 (2021) 117552, https://doi.org/10.1016/j.applthermaleng.2021.117552.
[16] S.H. Ammar, N.N. Ismail, A.D. Ali, W.M. Abbas, Electrocoagulation technique for refinery wastewater treatment in an internal loop split-plate airlift reactor, *J. Environ. Chem. Eng.* 7 (6) (2019) 103489, https://doi.org/10.1016/j.jece:2019.103489.
[17] J. Pan, et al., Experimental and numerical study on the transition conditions and influencing factors of hetero-/homogeneous reaction for H2/Air mixture in micro catalytic combustor, *Appl. Therm. Eng.* 154 (2019) 120–130, https://doi.org/10.1016/j.applthermaleng.2019.03.076.
[18] H. Shang, G. Xia, L. Cheng, S. Miao, Comprehensive review of enhancement techniques and mechanisms for flow boiling in micro/mini-channels, *Appl. Therm. Eng.* 258 (2025) 124783, https://doi.org/10.1016/j.applthermaleng.2024.124783.
[19] Z.M. Marouf, M.A. Fouad, M.A. Hassan, Experimental investigation of the effect of air bubbles injection on the performance of a plate heat exchanger, *Appl. Therm. Eng.* 217 (2022) 119264, https://doi.org/10.1016/j.applthermaleng.2022.119264.
[20] S. Roy, M.T. Dhotre, J.B. Joshi, CFD simulation of flow and axial dispersion in external loop airlift reactor, *Chem. Eng. Res. Des.* 84 (8) (2006) 677–690, https://doi.org/10.1205/cherd.05178.
[21] A. Hekmat, A.E. Amooghin, M.K. Moraveji, CFD simulation of gas–liquid flow behaviour in an air-lift reactor: determination of the optimum distance of the draft tube, *Simul. Model. Pract. Theory* 18 (7) (2010) 927–945, https://doi.org/10.1016/j.simpat.2010.02.009.
[22] M. Ebrahimifakhar, E. Mohsenzadeh, S. Moradi, M. Moraveji, M. Salimi, CFD simulation of the hydrodynamics in an internal air-lift reactor with two different configurations, *Front. Chem. Sci. Eng.*, 5 (4) (2011) 455–462, https://doi.org/10.1007/s11705-011-1116-x.
[23] M. Šimčík, A. Mota, M.C. Ruzicka, A. Vicente, J. Teixeira, CFD simulation and experimental measurement of gas holdup and liquid interstitial velocity in internal loop airlift reactor, *Chem. Eng. Sci.* 66 (14) (2011) 3268–3279, https://doi.org/10.1016/j.ces.2011.01.059.
[24] Y. Xu, L. Luo, J. Yuan, CFD simulations to portray the bubble distribution and the hydrodynamics in an annulus sparged air-lift bioreactor, *Can J Chem Eng* 89 (2) (2011) 360–368, https://doi.org/10.1002/cjce:20405.
[25] A. Ebadi Amooghin, S. Jafari, H. Sanaeepur, A. Kargari, Computational fluid dynamics simulation of bubble coalescence and breakup in an internal airlift reactor: analysis of effects of a draft tube on hydrodynamics and mass transfer, *Appl. Math. Model.* 39 (5–6) (2015) 1616–1642, https://doi.org/10.1016/j.apm.2014.09.020.
[26] L. Chen, Z. Bai, CFD simulation of the hydrodynamics in an industrial scale cyclohexane oxidation airlift loop reactor, *Chem. Eng. Res. Des.* 119 (2017) 33–46, https://doi.org/10.1016/j.cherd.2017.01.008.
[27] N. Farhadian, J. Behin, A. Parvareh, Residence time distribution in an internal loop airlift reactor: CFD simulation versus digital image processing measurement, *Comput. Fluids* 167 (2018) 221–228, https://doi.org/10.1016/j.compfluid.2018.02.030.
[28] N. Moudoud, R. Rihani, F. Bentahar, J. Legrand, Global hydrodynamic of hybrid external loop airlift reactor: experiments and CFD modelling, *Chem. Eng. Process. - Process Intesif.* 129 (2018) 118–130, https://doi.org/10.1016/j.cep.2018.05.005.
[29] S. Kouzbour, Y. Stiriba, B. Gourich, C. Vial, CFD simulation and analysis of reactive flow for dissolved manganese removal from drinking water by aeration process using an airlift reactor, *J. Water Process Eng.* 36 (2020) 101352, https://doi.org/10.1016/j.jwpe.2020.101352.
[30] X. Li, G. Zhang, X. Zhao, J. Zhou, G. Du, J. Chen, A conceptual air-lift reactor design for large scale animal cell cultivation in the context of in vitro meat production, *Chem. Eng. Sci.* 211 (2020) 115269, https://doi.org/10.1016/j.ces.2019.115269.
[31] R. Salehpour, E. Jalilnejad, M. Nalband, K. Ghasemzadeh, Hydrodynamic behavior of an airlift reactor with net draft tube with different configurations: numerical evaluation using CFD technique, *Particuology* 51 (2020) 91–108, https://doi.org/10.1016/j.partic.2019.09.005.
[32] S.M. Teli, C.S. Mathpati, Experimental and numerical study of gas-liquid flow in a sectionalized external-loop airlift reactor, *Chin. J. Chem. Eng.* 32 (2021) 39–60, https://doi.org/10.1016/j.cjche.2020.10.023.
[33] M.W. Abdulrahman, CFD simulations of direct contact volumetric heat transfer coefficient in a slurry bubble column at a high gas temperature of a helium–water–alumina system, *Appl. Therm. Eng.* 99 (2016) 224–234, https://doi.org/10.1016/j.applthermaleng.2016.01.043.
[34] J.J. Heijnen, J. Hols, R.G.J.M. Van Der Lans, H.L.J.M. Van Leeuwen, A. Mulder, R. Weltevrede, A simple hydrodynamic model for the liquid circulation velocity in a full-scale two- and three-phase internal airlift reactor operating in the gas recirculation regime, *Chem. Eng. Sci.* 52 (15) (1997) 2527–2540, https://doi.org/10.1016/S0009-2509(97)00070-5.
[35] E. Camarasa, et al., Development of a complete model for an air-lift reactor, *Chem. Eng. Sci.* 56 (2) (2001) 493–502, https://doi.org/10.1016/S0009-2509(00)00253-0.
[36] C. Vial, S. Poncin, G. Wild, N. Midoux, Experimental and theoretical analysis of the hydrodynamics in the riser of an external loop airlift reactor, *Chem. Eng. Sci.* (2002).
[37] R.D. Felice, Liquid circulation rates in two- and three-phase external airlift reactors, *Chem. Eng. J.* 109 (1–3) (2005) 49–55, https://doi.org/10.1016/j.cej.2005.03.009.
[38] E. Burlutskii, R. Di Felice, Experimental and numerical study of two-phase flow mixing in gas–liquid external-loop airlift reactor, *Int. J. Multiph. Flow* 119 (2019) 1–13, https://doi.org/10.1016/j.ijmultiphaseflow.2019.07.007.
[39] G. Brambati, M. Guilizzoni, S. Foletti, Convective heat transfer correlations for Triply Periodic Minimal Surfaces based heat exchangers, *Appl. Therm. Eng.* 242 (2024) 122492, https://doi.org/10.1016/j.applthermaleng.2024.122492.
[40] S. Kakaç, H. Liu, *Heat exchangers: selection, rating, and thermal design*, 2. ed., CRC Press, Boca Raton, Fla, 2002.
[41] B.R. Munson, D.F. Young, T.H. Okiishi, *Fluid mechanics*, 4th ed., John Wiley & Sons Inc, 2002.
[42] M. Ishii, T. Hibiki, *Thermo-fluid dynamics of two-phase flow*, Springer New York, New York, NY, 2011, 10.1007/978-1-4419-7985-8.
[43] J. Deng, et al., Experimental research and model development on interfacial drag in rectangle channel bubbly and slug flow, *Exp. Therm Fluid Sci.* 130 (2022) 110506, https://doi.org/10.1016/j.expthermflusci.2021.110506.
[44] W.R. Lockhart, Proposed correlation of data for isothermal two-phase, two-component flow in pipes, *Chem. Eng. Prog.* 45 (1) (1949) 39–48.
[45] D. Chisholm, A theoretical basis for the Lockhart-Martinelli correlation for two-phase flow, *Int. J. Heat Mass Transf.* 10 (12) (1967) 1767–1778, https://doi.org/10.1016/0017-9310(67)90047-6.
[46] A. Faghri, Y. Zhang, *Fundamentals of multiphase heat transfer and flow*, Springer International Publishing, Cham, 2020, 10.1007/978-3-030-22137-9.